Two-level Coupling-based Frequency Control Strategy with Adaptive Distributed Frequency Consensus and Dynamic Compensation

Congyue Zhang, *Member*, *IEEE*, Xiaobo Dou, *Senior Member*, *IEEE*, Jianfeng Zhao, Qinran Hu, *Senior Member*, *IEEE*, and Xiangjun Quan, *Member*, *IEEE*

Abstract—**This paper highlights the inefficiency of most distributed controls in dealing with dynamic enhancement while coordinating distributed generators (DGs), leading to poor frequency dynamics. To address this concern, a two-level coupling-based frequency control strategy for microgrids is proposed in this paper. At the lower level, an adaptive dynamic compensation algorithm is designed to tackle short-term and long-term frequency fluctuations caused by the uncertainties of renewable energy resources (RESs). At the upper level, an adaptive distributed frequency consensus algorithm is developed to address frequency restoration and active power sharing. Furthermore, to account for the potential control interaction of the two designed levels, a nonlinear extended state observer (NESO) is introduced to couple their control dynamics. Simulation tests and hardware-in-the-loop (HIL) experiments confirm the improved frequency dynamics.**

Index Terms—**Microgrid, frequency control, inertia, dynamic compensation, distributed control.**

I. INTRODUCTION

THE growing application of converter-interfaced renewable energy resources (RESs) imposes new challenges to the control of microgrids [1], [2]. In conventional islanded microgrids, droop-controlled distributed generators (DGs) are widely adopted at the primary layer to support frequency, ensure voltage level, and achieve reasonable power sharing [3]. However, to ensure fast response dynamics, traditional droop control only mimics the droop property of synchronous generators (SGs), making it challenging to provide sufficient inertia for microgrids. The lack of inertia can cause faster frequency dynamics, making the microgrids suffer from high rate of change of frequency (RoCoF) under disturbances and uncertainties. Besides, significant fluctuations of RESs can also increase the frequency nadir due to the low damping characteristic, which may trigger protection actions and lead to outages throughout the microgrids [4]. Therefore, inertia compensation and frequency restoration technologies have become research hotspots in recent years.

Sufficient inertia is especially essential at the beginning of disturbance for restraining severe frequency fluctuations [5]-[7]. In this context, to compensate for inertia, the concept of virtual synchronous generator (VSG) has been proposed by mimicking the swing equation of SGs [8]. In recent years, to implement stable inertia compensation, researchers have conducted many detailed discussions on parameter configuration [9], [10], compensation efficiency [11]-[13], and control stability [14]-[16] of VSGs. References [9] and [10] discuss the compensation of both inertia and damping, and give guidance for parameter configuration. In [12] and [13], model predictive control (MPC) and data-driven strategies have been adopted by VSGs to obtain satisfactory response characteristics. However, the same as the droop control process, the VSG control process is also integrated into the primary control of DGs. The commercial setup of DGs makes it challenging to adjust inertia parameters according to different operating conditions.

To compensate for inertia in a more flexible manner, inertia emulation controls have received much attention recently. Unlike the VSG control, inertia emulation control compensates for inertia by developing additional outer feedback loops. For example, [17] and [18] propose extended virtual inertia control for energy storage systems (ESSs) and photovoltaic (PV) systems to compensate for inertia, and adopt robust controls to optimize the compensation results. In the same way, [19] and [20] introduce virtual inertia control loops for ESSs and employ MPC to optimize compensation coefficients. However, inertia emulation relies on fast feedback of RoCoF in a very instant time. The direct design of outer inertia loop in the secondary control layer [17]-[20] and ignorance of the dynamics of the primary layer may lead to untimely compensations or low-frequency oscillations caused by decoupling the executions of two layers.

Manuscript received: July 23, 2023; revised: November 10, 2023; accepted: February 8, 2024. Date of CrossCheck: February 8, 2024. Date of online publication: March 22, 2024.

This work was supported in part by the Jiangsu Funding Program for Excellent Postdoctoral Talent (No. 2023ZB391), in part by the China Postdoctoral Science Foundation (No. 2023M740588), and in part by the National Natural Science Foundation of China (No. 52077036).

C. Zhang, X. Dou (corresponding author), J. Zhao, Q. Hu, and X. Quan are with the School of Electrical Engineering, Southeast University, Nanjing 210096, China, and J. Zhao is also with the College of Information Science and Technology & Artificial Intelligence, Nanjing Forestry University, Nanjing 210037, China (e-mail: zhangcongyue1993@outlook.com; dxb_2001@sina.com; jianfeng_zhao@seu.edu.cn; qhu@seu.edu.cn; qxj@seu.edu.cn).

DOI: 10.35833/MPCE.2023.000506

In addition to sufficient inertia support, it is also crucial to match the inertia and damping compensations to the operation dynamics for the sake of power system stability. Unlike the plannable power generation from SGs, the power outputs of RESs are uncertain and periodic, causing the power system to simultaneously face unpredictable fluctuations in a short timescale and periodic outputs in a long timescale [21]. In power systems with high integration of photovoltaic (PV), power flow varies significantly between noon and midnight. The inertia required at night can be much less than at other period of the day (especially at noon) [6]. Mismatched inertia compensations can degrade the dynamics of the control system and even cause instability.

For islanded microgrids, distributed and centralized controls are the two typical practices to eliminate frequency deviation and achieve accurate power sharing. Centralized control coordinates distributed resources through centralized collection and interaction. This allows for high control accuracy and the ability to obtain a globally optimal solution. However, due to the complex communication and centralized calculation involved, it suffers from low efficiency and instability [22]. In contrast, distributed control only exchanges data with neighbors and calculates locally, which significantly increases the control resilience [23]. In recent years, various algorithms have been adopted by distributed control to address related issues. For example, finite-time control algorithms are adopted by [24]-[28] to reduce the frequency convergence time. References [29] and [30] discuss the impacts of sensor/actuator faults on control performance. In addition, the delay and bandwidth issues are investigated in [31] and [32]. However, although most distributed controls employ DGs as the control objects, most consensus designs still ignore the reduced inertia and degraded frequency dynamics caused by integrated RESs and droop-controlled DGs.

Therefore, inspired by the above-mentioned limitations, this paper proposes a novel frequency control strategy to enhance frequency stability while addressing rapid restoration. The major contributions can be summarized as follows.

1) A two-level coupling-based frequency control strategy is developed in this paper. The proposed distributed controller includes an adaptive frequency consensus algorithm and a dynamic compensation algorithm, which allows the controller to achieve frequency consensus, accurate power sharing, and dynamic enhancement simultaneously.

2) A nonlinear extended state observer (NESO) is adopted to couple the dynamics in different control levels. The NESO can eliminate more than ten times the decoupling time between different levels, which makes the system responses faster and better handles uncertainties than the decoupling methods in [17]-[20], [33], especially at the beginning of disturbances.

3) An adaptive dynamic compensation algorithm is developed for DGs. Compared with the traditional fixed inertia compensations [3], [17]-[20], the adaptive dynamic compensation algorithm can better handle fast and periodic fluctuations. Additionally, the external feedback design can better deal with the difficulty in adjusting parameters in DGs.

4) An adaptive distributed frequency consensus algorithm is proposed to facilitate rapid frequency consensus and ensure precise power sharing. The adaptive convergence design incorporated in the algorithm can expedite the recovery rate at far ends and minimize the chattering near equilibrium points.

II. PRELIMINARIES

A. Graph Theory

A system composed of one leader and N following droop-controlled DGs is considered in this paper. We employ an undirected graph $G=\{\boldsymbol{V},\boldsymbol{E},\boldsymbol{A}\}$ to express the communication topology between DGs, where $\boldsymbol{V}=\{1,2,\dots,N\}$ is the agent set, $\boldsymbol{E}=\{(i,j), i,j\in V\}$ is the edge set, and $\boldsymbol{A}=[a_{ij}]_{N\times N}$ is the adjacency matrix. If there is an information flow from DG$_i$ to DG$_j$, we can have $a_{ij}=a_{ji}=1$; otherwise, $a_{ij}=a_{ji}=0$. The matrix $\boldsymbol{L}=[l_{ij}]_{N\times N}$ with elements $l_{ij}=-a_{ij}$ if $j\neq i$; otherwise, $l_{ii}=\sum_{i-1}^{N} a_{ij}$ are the elements of the Laplacian matrix of G.

We adopt $\boldsymbol{B}=\mathrm{diag}\{b_1,b_2,\dots,b_N\}$ as the leader matrix to describe the communication connection relationship between DGs and the leader, in which $b_i>0$ represents the existing information flow from the leader to DGi [3], [30].

B. Basic Control Model of DGs

Figure 1 illustrates the control structure of droop-controlled DGs, where Q_i is the output reactive power; Q_i^* is the measured filtered reactive power; i_i is the output current; i' is the current reference; and L_{fi}, R_{fi} and C_{fi} are the inductance, resistance and capacitance of the LC filter, respectively. The droop function of frequency control is described as:

$$\omega_i=\omega_{ref,i}-m_{Pi}P_i^* \tag{1}$$

where ω_i is the output frequency; $\omega_{ref,i}$ is the frequency control reference; P_i^* is the measured filtered active power; and m_{Pi} is the droop coefficient.

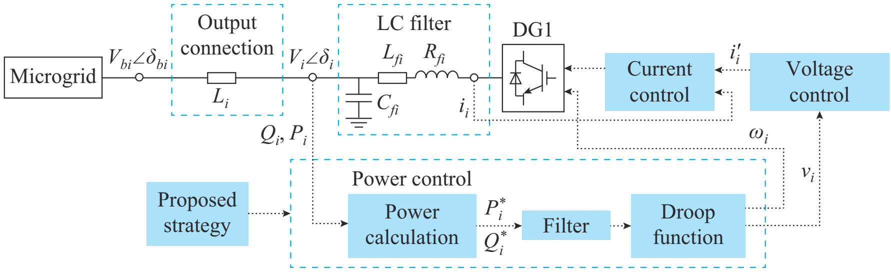

Fig. 1. Control structure of droop-controlled DGs.

The filtered active power can be expressed as (2), which yields (3).

$$P_i^* = \frac{1}{\tau_i s + 1} P_i \tag{2}$$

$$\tau_i \dot{P}_i^* = -P_i^* + P_i \tag{3}$$

where $\dot{P}_i^*$ is the derivative of the filtered active power P_i^*; P_i is the real output active power; τ_i is the time constant of the first-order low-pass filter; $1/(\tau_i s + 1)$ is the filter process; and s is the Laplace operator.

Combining (1) and (2), the frequency dynamics can be expressed as [34]:

$$\begin{cases} \tau_i \dot{\omega}_i = -m_{Pi} P_i - (\omega_i - u_{ref,i}) \\ u_{ref,i} = \tau_i \dot{\omega}_{ref,i} + \omega_{ref,i} \end{cases} \tag{4}$$

where $u_{ref,i}$ is the introduced control reference from the secondary layer. Its relationship with the frequency control reference is expressed as $\omega_{ref,i} = 1/(\tau_i s + 1) u_{ref,i}$, which can be obtained by first-order filtering.

To simultaneously address frequency restoration, active power sharing, and dynamic compensation, the introduced control reference is divided into two components:

$$u_{ref,i} = u^{\omega}_{ac,i} + u^{\omega}_{dc,i} \tag{5}$$

where $u^{\omega}_{ac,i}$ is the reference from adaptive compensation; and $u^{\omega}_{dc,i}$ is the frequency reference from distributed consensus.

Remark 1: comparing (4) with the second-order swing equation, a droop-controlled DG is mathematically identical to an SG with small inertia τ_i / m_{Pi}.

C. Control Structure

The control structure of the proposed strategy is given in Fig. 2. We adopt droop-controlled DGs as the objects, which is the same as most distributed control [24]-[32].

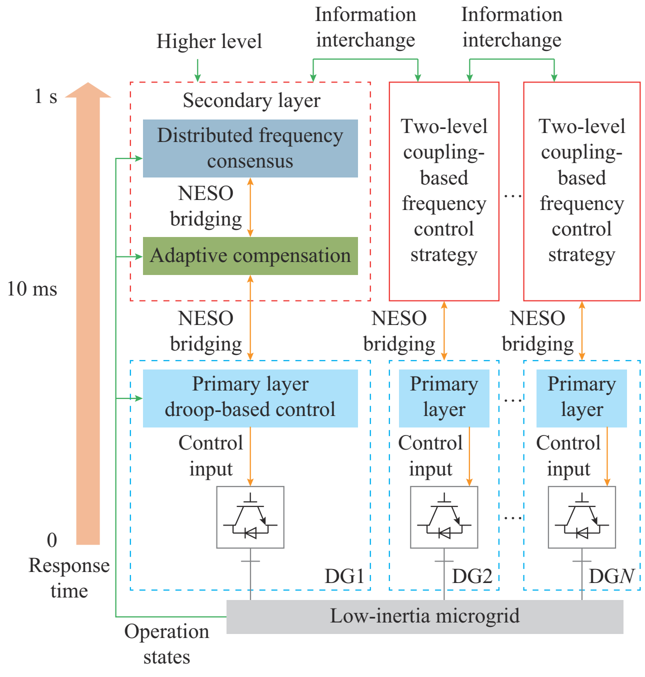

Fig. 2. Control structure of proposed strategy.

The adaptive compensation and the adaptive sliding model (ASM)-based distributed frequency consensus are designed and coupled in secondary controllers. The NESO is introduced to couple the dynamics in the primary and secondary layers.

III. TWO-LEVEL COUPLING-BASED FREQUENCY CONTROL STRATEGY

A. Adaptive Dynamic Compensation

Conventional droop control (4) cannot provide sufficient inertia or damping to microgrids, which will easily result in rapid frequency fluctuations after disturbances. In addition, conventional strategies such as single- and fixed-coefficient inertia compensation are insufficient in dealing with fast frequency and periodic fluctuations.

To compensate for inertia and damping flexibly, we introduce the adaptive dynamic compensation as:

$$u^{\omega}_{ac,i}(t) = \mu_1 \omega_{di}(t) (\dot{\omega}_{di}(t))^2 + \mu_2 P_F(t) \omega_{di}(t) \tag{6}$$

where $\omega_{di}(t) = \omega_i(t) - u^{\omega}_{dc,i}(t)$ is the defined frequency consensus tracking deviation; μ_1 and μ_2 are the positive constant coefficients; and $P_F(t) \geq 0$ is the rough day-ahead power forecast given by the higher layer.

Remark 2: for adaptive compensation design (6), the first component $\mu_1 \omega_{di}(t) (\dot{\omega}_{di}(t))^2$ is the inertia compensation, which can reduce the RoCoF when the frequency deviates from the steady state, and can accelerate the restoration rate when the frequency is back to the steady state [21]. The second component $\mu_2 P_F(t) \omega_{di}(t)$ is the periodicity damping compensation, which can avoid large frequency overshoots or drops at noon or night.

The short-term compensation mechanism of $\mu_1 \omega_{di}(t) \dot{\omega}_{di}(t)$ is given in Fig. 3(a). The periodicity compensation mechanism $\mu_2 P_F(t)$ is given in Fig. 3(b).

By introducing (6) in (4), the frequency dynamics can be remodelled as:

$$(\tau_i + \mu_1 \omega_{di}(t) \dot{\omega}_{di}(t)) \dot{\omega}_{di}(t) + (\mu_2 P_F(t) + 1) \omega_{di}(t) = -m_{Pi} P_i(t) \tag{7}$$

Assumption 1: the output connection of the investigated DGs is highly inductive.

Theorem 1: under Assumption 1, the proposed adaptive dynamic compensation (6) can stably compensate for inertia and damping to DGs. Proof can be found in Appendix A.

In addition, to ensure that compensation strengthens the frequency dynamics instead of degrading them, the following parameter constraints of μ_1 and μ_2 are discussed.

After introducing the adaptive dynamic compensation, the inertia $J_i(t)$ and damping coefficient $D_i(t)$ of DGs can be expressed as:

$$\begin{cases} J_i(t) = \dfrac{\mu_1 \omega_{di}(t) \dot{\omega}_i(t) + \tau_i}{m_{Pi}} \\ D_i(t) = \dfrac{\mu_2 P_F(t) + 1}{m_{Pi}} \end{cases} \tag{8}$$

Then, the crossover frequency $\omega_{c,i}(t)$ and damping ratio $\xi_i(t)$ of the compensated DG can be given as:

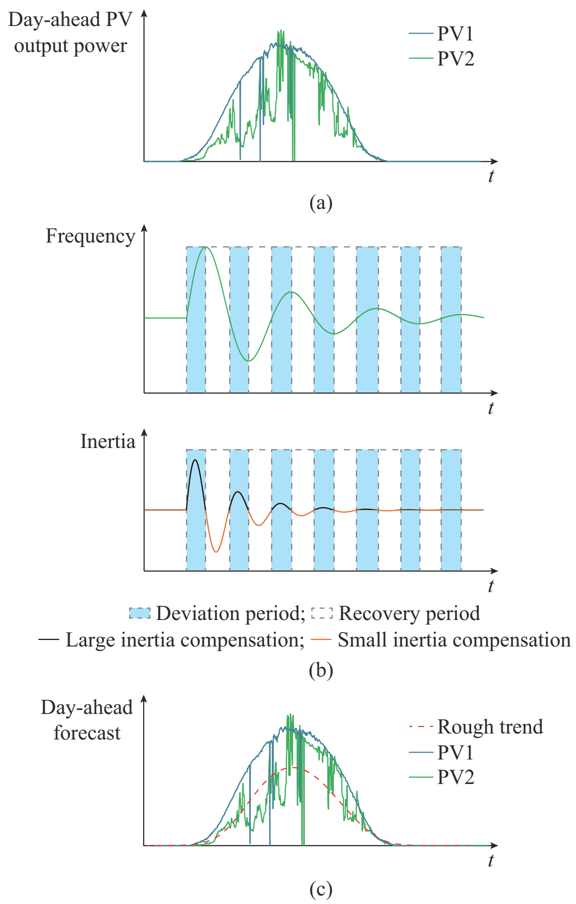

Fig. 3. Adaptive compensation mechanism. (a) Day-ahead PV output power. (b) Short-term compensation. (c) Long-term compensation.

$$\begin{cases}\omega_{c,i}(t)=\dfrac{1}{4}\sqrt{-\eta_i^2(t)+\sqrt{\eta_i^4(t)+4A_i^2/J_i^2(t)}}\\ \xi_i(t)=\dfrac{D_i(t)}{2\sqrt{J_i(t)A_i}}\end{cases} \tag{9}$$

where $\eta_i(t)=D_i(t)/J_i(t)$ is the damping-inertia ratio; and A_i is a defined coefficient in Appendix A.

To enhance the operation dynamics against disturbances, the crossover frequency should be ideally placed ten times below the nominal grid frequency $\omega_{grid}(t)$ to remove the effects of line resonance [9]. Besides, the damping ratio should be larger than one to eliminate overshoots and oscillations.

$$\begin{cases}\omega_{c,i}(t)\le 0.1\omega_{grid}(t)\\ \xi_i(t)\ge 1\end{cases} \tag{10}$$

By solving (10), we can obtain the following results.

$$\begin{cases}0<\mu_1\le\left(\dfrac{1}{4A_i}-\tau_i\right)\dfrac{1}{\left|\omega_{di}(t)\dot{\omega}_{di}(t)\right|_{\max}}\\ \mu_2\ge\dfrac{1}{\left|P_F(t)\right|_{\max}}\left(10\sqrt{\sqrt{5}+2}\,\dfrac{A_i}{\omega_{grid}(t)}-1\right)\end{cases} \tag{11}$$

According to stability proof and parameter calculation, the proposed adaptive dynamic compensation can achieve the dynamic enhancement in a stable and efficient manner.

B. Simplification of Control Model by NESO

The frequency dynamics are nonlinear, as shown in (7). This subsection aims to simplify the control model by the NESO without decoupling the controls in different layers.

A second-order control model is given in (12) with the control states y_1 and y_2, control input u, control gain b, and function f.

$$\begin{cases}\dot{y}_1=y_2\\ \dot{y}_2=f(y_1,y_2)+bu\end{cases} \tag{12}$$

A typical NESO can address the observation of the nonlinear and state parts, which can be given as [35]:

$$\boldsymbol{y}=[\hat{y}_1,\ \hat{y}_2,\ \hat{y}_3]^{\mathrm{T}}\rightarrow[y_1,\ y_2,\ f(y_1,y_2)]^{\mathrm{T}} \tag{13}$$

where $\hat{y}_1$, $\hat{y}_2$, and $\hat{y}_3$ are the observed states of y_1, y_2, and y_3, respectively.

Based on the established frequency dynamics, we have:

$$(\tau_i+\mu_1\omega_{di}(t)\dot{\omega}_{di}(t))\dot{\omega}_{di}(t)+(\mu_2P_F(t)+1)\omega_{di}(t)=-m_{Pi}P_i(t)+w_i \tag{14}$$

where w_i is an additional state to represent the unmodeled uncertainties of DGs and the unknown frequency/voltage coupling in microgrids.

Let us denote vectors $[x_{i,1}(t),\ x_{i,2}(t)]^{\mathrm{T}}=[\omega_{di}(t),\ \dot{\omega}_{di}(t)]^{\mathrm{T}}$, $[y_{i,1}(t),\ y_{i,2}(t)]^{\mathrm{T}}=[\omega_i(t),\ \dot{\omega}_i(t)]^{\mathrm{T}}$, and an auxiliary input state $u_i(t)$. We can simplify the derivative of (14) as:

$$\begin{cases}\dot{y}_{i,1}(t)=y_{i,2}(t)\\ \dot{y}_{i,2}(t)=f(x_{i,2}(t),x_{i,1}(t))+b_{\omega,i}u_i(t)\\ u_i(t)=(\mu_2P_F(t)+1)\dot{u}_{dc,i}^{\omega}(t)-m_{Pi}\dot{P}_i(t)\end{cases} \tag{15}$$

where $b_{\omega,i}=1/\tau_i$ is the defined control gain; and the nonlinear part $f(x_{i,2}(t),x_{i,1}(t))$ is given as:

$$\begin{aligned}f(x_{i,2}(t),x_{i,1}(t))=-b_{\omega,i}[&2\mu_1\dot{x}_{i,2}(t)x_{i,2}(t)x_{i,1}(t)+\mu_1x_{i,2}^3(t)+\\ &(\mu_2P_F(t)+1)\dot{\omega}_i(t)-\mu_2\dot{P}_F(t)x_{i,1}(t)-\dot{w}_i]\end{aligned} \tag{16}$$

Based on (13), we can have the observation results as $\hat{y}_{i,3}(t)\rightarrow f(x_{i,1}(t),\ x_{i,2}(t))$, $\hat{y}_{i,2}(t)\rightarrow\dot{\omega}_{di}(t)$, $\hat{y}_{i,1}(t)\rightarrow\omega_{di}(t)$.

Finally, the frequency control model of the i^{th} DG with adaptive compensations is reformulated as:

$$\begin{cases}\dot{\hat{y}}_{i,1}(t)=\hat{y}_{i,2}(t)\\ \dot{\hat{y}}_{i,2}(t)=\hat{y}_{i,3}(t)+b_{\omega,i}u_i(t)\end{cases} \tag{17}$$

Remark 3: the control of DGs is complicated. Thus, the NESO is adopted in this paper to simplify the complicated model of DGs to a second-order form (15). In this simplified model, we only retain the main processes directly related to the frequency control. The intermediate and coupling processes are separated by means of observation.

Remark 4: adopting NESO to simplify the system model can preserve the entire dynamics of the DG. Compared with the traditional time decoupling design adopted by the multilevel system, it can avoid the selection and rejection of some specific fast dynamics, and prevent the slow response speed caused by time decoupling control between different levels.

C. Adaptive Distributed Frequency Consensus and Active Power Sharing

This subsection aims to address adaptive distributed frequency consensus, i.e., $\omega_i(t)\rightarrow\omega_n$, where ω_n is the global frequency reference, and accurate power sharing, i. e., $m_{Pj}P_j(t) \rightarrow m_{Pi}P_i(t)$.

First, to solve the fast-frequency consensus among DGs in the microgrid, we define tracking errors $e_{i,1}$ and $e_{i,2}$ as:

$$e_{i,1}(t-d_i) = \sum_{j=1}^{N} a_{ij}(\hat{y}_{i,1}(t-d_i) - \hat{y}_{j,1}(t-d_i)) + b_i(\hat{y}_{i,1}(t-d_i) - \omega_n) \tag{18}$$

$$e_{i,2}(t-d_i) = \sum_{j=1}^{N} a_{ij}(\hat{y}_{i,2}(t-d_i) - \hat{y}_{j,2}(t-d_i)) + b_i \hat{y}_{i,2}(t-d_i) \tag{19}$$

where $d_i = \max\{d_{ij}\}$, and d_{ij} is the communication delay between DG_i and DG_j.

To address rapid frequency convergence, a sliding manifold is designed as:

$$s_i(t) = e_{i,2}(t) + k_1 e_{i,1}(t) \tag{20}$$

where k_1 is a positive coefficient.

Then, the time derivative of $s_i(t)$ is expressed as:

$$\dot{s}_i(t) = \dot{e}_{i,2}(t) + k_1 e_{i,2}(t) \tag{21}$$

Lemma 1 (see [36]): since k_1 is a positive value and $\dot{e}_{i,1}(t) = e_{i,2}(t)$, the frequency consensus objective $e_{i,1}(t) \rightarrow 0$ is equal to the objective of $s_i(t-d_i) \rightarrow s_i(t) \rightarrow 0$.

To accelerate the convergence rate at the far end and avoid chattering near the equilibrium, an adaptive reaching law is designed as:

$$\dot{s}_i(t) = -\gamma_{\omega,i}(t-d_i)\left|s_i(t-d_i)\right|\kappa(\gamma_{\omega,i}(t-d_i), s_i(t-d_i)) - \eta_{\omega,i}s_i(t) \tag{22}$$

where $\eta_{\omega,i}$ is a positive constant; and the nonlinear function $\kappa(\gamma_{\omega,i}(t-d_i), s_i(t-d_i))$ is given as:

$$\kappa(\gamma_{\omega,i}(t-d_i), s_i(t-d_i)) = \begin{cases} \operatorname{sign}(s_i(t-d_i)) & \gamma_{\omega,i}(t-d_i)\left|s_i(t-d_i)\right| \geq \vartheta \\ \gamma_{\omega,i}(t-d_i)\dfrac{s_i(t-d_i)}{\vartheta} & \gamma_{\omega,i}(t-d_i)\left|s_i(t-d_i)\right| < \vartheta \end{cases} \tag{23}$$

where ϑ is a small positive constant; and the state $\gamma_{\omega,i}(t)$ is an adaptive coefficient, which is shown by (24). It can accelerate the convergence rate when the state $s_i(t)$ is at the far end.

$$\gamma_{\omega,i}(t-d_i) = -\frac{1}{\lambda_{\omega,2}}\left(\dot{\gamma}_{\omega,i}(t-d_i) + \lambda_{\omega,1}\left|s_i(t-d_i)\right|^2\right) \tag{24}$$

Based on the graph theory, the global vector form of (20) is expressed as:

$$\boldsymbol{s}(t) = (\boldsymbol{L}+\boldsymbol{B})[\boldsymbol{y}_2(t) + k_1(\boldsymbol{y}_1(t) - \boldsymbol{I}_N\omega_n)] \tag{25}$$

where $\boldsymbol{y}_1(t)$ is the global vector form of $\hat{y}_{i,1}(t)$; $\boldsymbol{y}_2(t)$ is the global vector form of $\hat{y}_{i,2}(t)$; and $\boldsymbol{I}_N$ is the unit vector.

Based on (20)-(25), the vector-form frequency control reference is written as:

$$\begin{aligned} \boldsymbol{u}(t) = -\Big[&\boldsymbol{\gamma}(t-d)\left|\boldsymbol{y}_2(t) + k_1(\boldsymbol{y}_1(t) - \boldsymbol{I}_N\omega_n)\right|\boldsymbol{\kappa}(\boldsymbol{\gamma}_\omega(t-d), \boldsymbol{s}(t-d)) + \\ &\boldsymbol{\eta}(\boldsymbol{y}_1(t) - \boldsymbol{I}_N\omega_n) + (k_1\boldsymbol{I}_{N\times N} + \boldsymbol{\eta})\boldsymbol{y}_2(t) + \boldsymbol{y}_3(t)\Big]\boldsymbol{T} \end{aligned} \tag{26}$$

where $\boldsymbol{\gamma}(t-d) = \operatorname{diag}\{\gamma_{\omega,1}(t-d_1), \gamma_{\omega,2}(t-d_2), \ldots, \gamma_{\omega,N}(t-d_N)\}$; $\boldsymbol{y}_3(t)$ is the vector form of $\hat{y}_{i,3}(t)$; $\boldsymbol{s}(t-d) = [s_1(t-d_1), s_2(t-d_2), \ldots, s_N(t-d_N)]^{\mathrm{T}}$; $\boldsymbol{T} = \operatorname{diag}\{\tau_1, \tau_2, \ldots, \tau_N\}$; and $\boldsymbol{\eta} = \operatorname{diag}\{\eta_{\omega,1}, \eta_{\omega,2}, \ldots, \eta_{\omega,N}\}$.

Then, the frequency control reference for the i^{th} DG can be expressed as:

$$\begin{aligned} u_i(t) = -\Big[&\gamma_{\omega,i}(t-d_i)\left|\hat{y}_{i,2}(t) + k_1(\hat{y}_{i,1}(t) - \omega_n)\right| \cdot \\ &\kappa(\gamma_{\omega,i}(t-d_i), s_i(t-d_i)) + \eta_{\omega,i}(\hat{y}_{i,1}(t) - \omega_n) + \\ &(k_1 + \eta_{\omega,i})\hat{y}_{i,2}(t) + \hat{y}_{i,3}(t)\Big]\tau_i \end{aligned} \tag{27}$$

Remark 5: in (27), the states $\hat{y}_{i,1}(t)$, $\hat{y}_{i,2}(t)$, and $\hat{y}_{i,3}(t)$ can be measured locally. The states $\gamma_{\omega,i}(t-d_i)$ and $s_i(t-d_i)$ require information from their neighbors for calculation, and are therefore subject to the impact of communication delays.

Based on (15) and (27), the control input from the distributed control can be expressed as:

$$u_{dc,i}^{\omega}(t) = \frac{1}{\mu_2 P_F(t) + 1}\left(\int u_i(t)\mathrm{d}t + m_{Pi}P_i(t)\right) \tag{28}$$

To further address the real power sharing among DGs, an auxiliary control $u_{i,ref}^{mp}(t)$ is defined as $u_{i,ref}^{mp}(t) = m_{Pi}\dot{P}_i(t)$ [25].

A similar result can be obtained for power sharing control as:

$$\begin{aligned} u_i^{mp}(t) = &-\gamma_{mp,i}(t-d_i)\left|m_{Pi}P_i(t)\right|\kappa(\gamma_{mp,i}(t-d_i), e_{i,mp}(t-d_i)) + \\ &\eta_{mp,i}m_{Pi}P_i(t) \end{aligned} \tag{29}$$

where the power sharing error $e_{i,mp}(t-d_i)$ and the adaptive state $\gamma_{mp,i}(t-d_i)$ are given as:

$$e_{i,mp}(t-d_i) = \sum_{j=1}^{N} a_{ij}(m_{Pi}P_i(t-d_i) - m_{Pj}P_j(t-d_i)) \tag{30}$$

$$\gamma_{mp,i}(t-d_i) = -\frac{1}{\lambda_{mp,2}}\left(\dot{\gamma}_{mp,i}(t-d_i) + \lambda_{mp,1}\left|e_{i,mp}(t-d_i)\right|^2\right) \tag{31}$$

where $\lambda_{mp,1}$, $\lambda_{mp,2}$, and $\eta_{mp,i}$ are the positive constant values.

Finally, combining (28) and (29), we can obtain the control input of the proposed strategy as:

$$u_{dc,i}^{\omega}(t) = \frac{1}{\mu_2 P_F(t) + 1}\left(\int u_i(t)\mathrm{d}t + u_i^{mp}(t)\right) \tag{32}$$

Theorem 2: employing the algorithms (27) and (29), the control input (32) can stably address frequency convergence and active power sharing among DGs under communication delay conditions. Proof can be found in Appendix B.

Figure 4 gives the control diagram of the proposed strategy.

IV. SIMULATION AND EXPERIMENTAL STUDIES

A microgrid modified according to the standard IEEE 34-bus system [3], [37], [38] with six DGs has been constructed, as shown in Fig. 5(a). The communication topology is given in Fig. 5(b).

The parameters of the DGs and loads are given in Table I and Table II, respectively. Subscript "*line*" indicates parameters of the output lines. The distributed controllers can exchange information with their neighbour controllers based on the data links. The control parameters are set as $\tau_i = 1\times 10^{-2}$, $\mu_1 = 0.2$, $\mu_2 = 6\times 10^{-2}$, $\vartheta = 10^{-3}$, $\lambda_{\omega,1} = 200$, $\lambda_{\omega,2} = 10$, $k_1 = 200$, and $\eta_{\omega,i} = 0.15$.

A. Case 1: Test of Basic Control Performance

Several scenarios are outlined in this subsection to test the basic control performance. The results shown in Figs. 6 and 7 indicate the control performance.

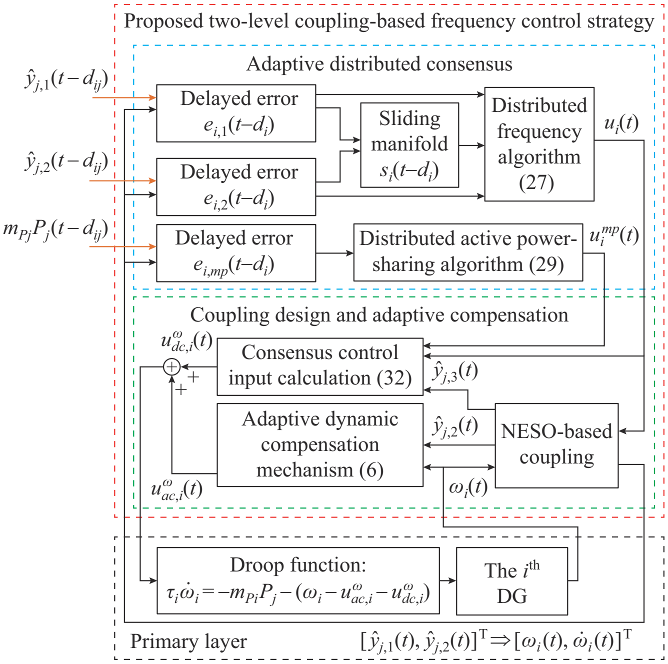

Fig. 4. Control diagram of proposed strategy.

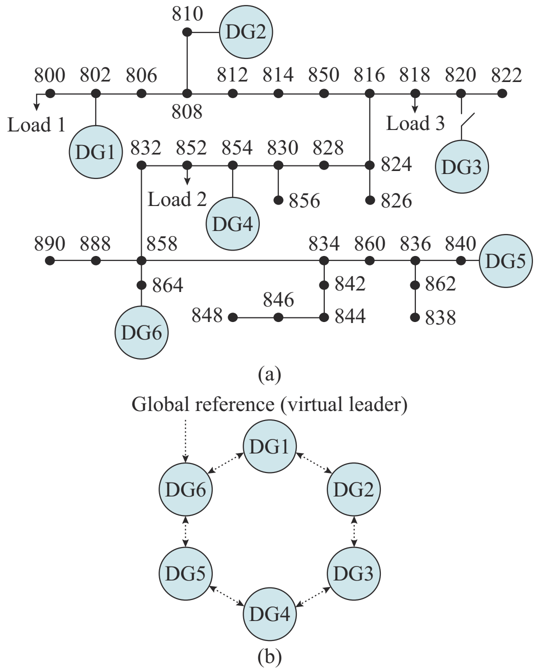

Fig. 5. Microgrid modified according to IEEE 34-bus system. (a) Microgrid. (b) Communication topology.

According to Fig. 6(a) and (b), prior to $t=1$ s, the microgrid is only engaged with droop control. The frequencies of DGs deviate from the nominal value. After the proposed strategy is triggered at $t=1$ s, the frequencies are recovered without affecting the droop-induced power sharing (Fig. 7(a)). Then, at $t=2$ s, the connected load 1 disconnects from the microgrid, and at $t=3$ s, the value of load 2 is doubled. The results shown in Figs. 6 and 7 illustrate that the proposed strategy can rapidly drive the frequencies of DGs back to the nominal value after the changes, and guarantee active power sharing among DGs.

TABLE I
PARAMETERS OF DGS

Symbol	Value	Symbol	Value	Symbol	Value
m_{p1}, m_{p6}	1×10^{-4}	m_{p2}	1.5×10^{-4}	m_{p3}, m_{p4}, m_{p5}	2×10^{-4}
n_{q1}, n_{q6}	5×10^{-4}	n_{q2}	7.5×10^{-4}	n_{q3}, n_{q4}, n_{q5}	10×10^{-4}
L_{f1}, L_{f6}	1.4 mH	L_{f2}	1.4 mH	L_{f3}, L_{f4}, L_{f5}	1.4 mH
C_{f1}, C_{f6}	50 μF	C_{f2}	50 μF	C_{f3}, C_{f4}, C_{f5}	50 μF
L_1, L_6	2.5 mH	L_2	3 mH	L_3, L_4, L_5	3 mH
R_{line1}, R_{line6}	0.25 Ω	R_{line2}	0.4 Ω	R_{line3}, R_{line4}, R_{line5}	0.35 Ω
L_{line1}, L_{line6}	30 mH	L_{line2}	38 mH	L_{line3}, L_{line4}, L_{line5}	40 mH

TABLE II
PARAMETERS OF LOADS

Symbol	Value	Symbol	Value	Symbol	Value
R_{L1}	1.5 Ω	R_{L2}	5.5 Ω	R_{L3}	3.8 Ω
L_{L1}	4.2 mH	L_{L2}	10.8 mH	L_{L3}	7.2 mH

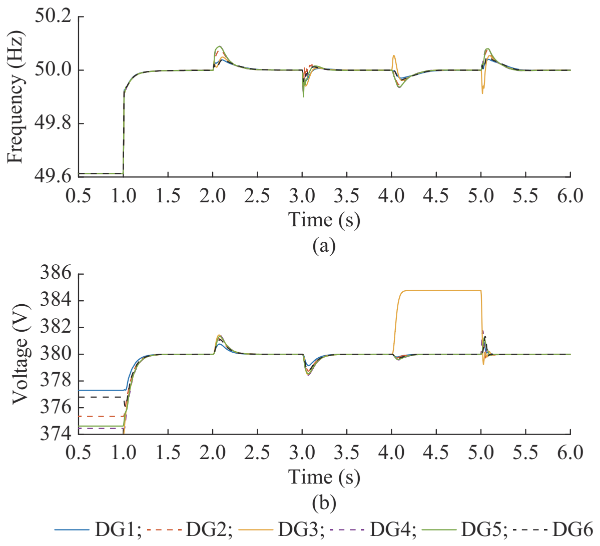

Fig. 6. Performance results of Case 1. (a) Frequency. (b) Voltage.

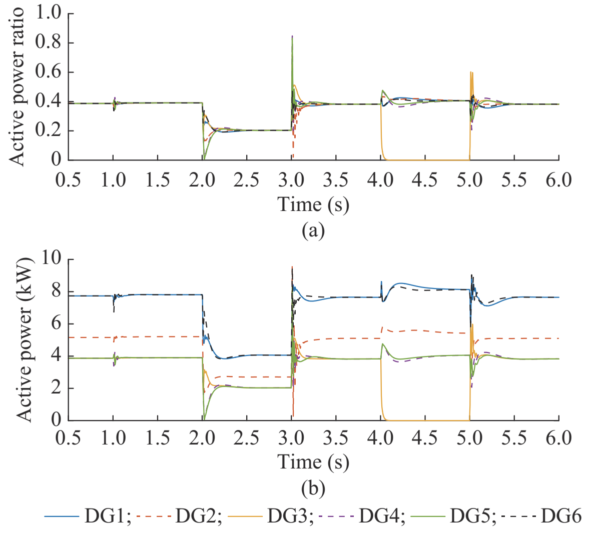

Fig. 7. Performance testing of Case 1. (a) Active power ratio. (b) Active power.

Next, at $t=4$ s and $t=5$ s, DG3 gets disconnected and connected in the microgrid, respectively. The results illustrate that the proposed strategy has a superior plug-and-play capacity to suppress the frequency overshot and ensure the control stability.

B. Case 2: Comparison of Control Performance

In this case, we compare our proposed strategy with the result in [26]. The comparison of different strategies for DG6 is given in Fig. 8. The proposed strategy has a faster convergence rate and lower frequency nadirs against disturbance than the common distributed control strategies.

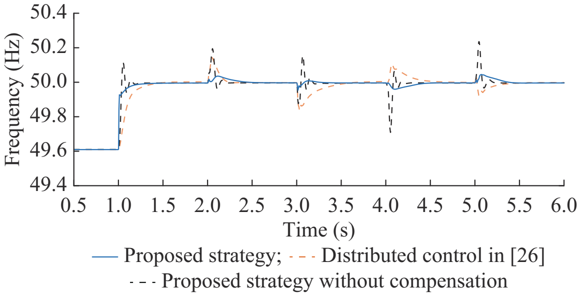

Fig. 8. Performance comparison of different strategies for DG6.

C. Case 3: Comparison with Time-decoupling Condition

The frequency control performance under time-decoupling conditions (without NESO coupling) is given in Fig. 9, and the comparison of the control performance is given in Fig. 10.

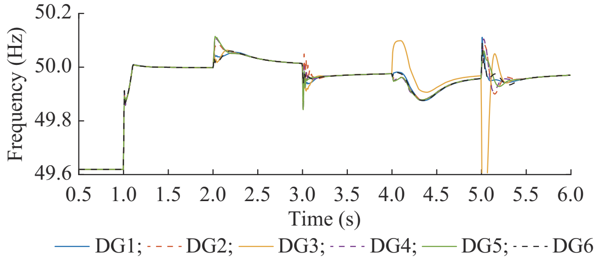

Fig. 9. Control performance under time-decoupling condition.

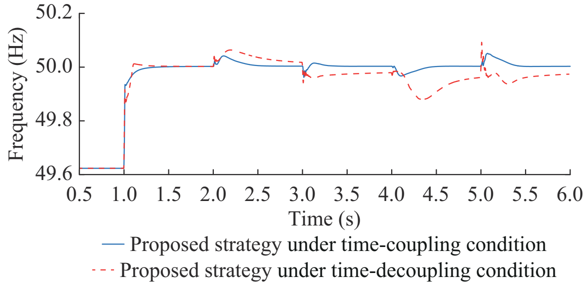

Fig. 10. Comparison of control performance.

Under the time-decoupling condition, the response time constants of different control levels are set to differ by 50 times to ensure the stability.

D. Case 4: Performance Under Different Delay Conditions

Two delay conditions are configured to test the effectiveness under communication delay conditions. Based on the linear programming problem (B7) and the control parameters setting, a feasible solution of the maximum delay can be calculated as $d_{\max}<\eta \rightarrow d_{\max}<150$ ms.

1) Delay condition 1: $d_{12}=40$ ms, $d_{23}=d_{34}=35$ ms, $d_{61}=25$ ms, $d_{45}=d_{56}=45$ ms.

2) Delay condition 2: $d_{12}=100$ ms, $d_{23}=d_{34}=95$ ms, $d_{61}=85$ ms, $d_{45}=d_{56}=105$ ms.

The results under different communication delay conditions are given in Figs. 11 and 12.

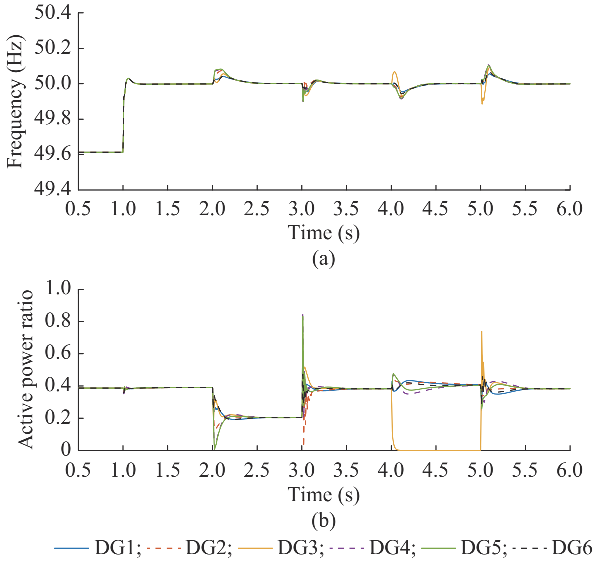

(a)

(b)

Fig. 11. Control performance under communication delay condition 1.

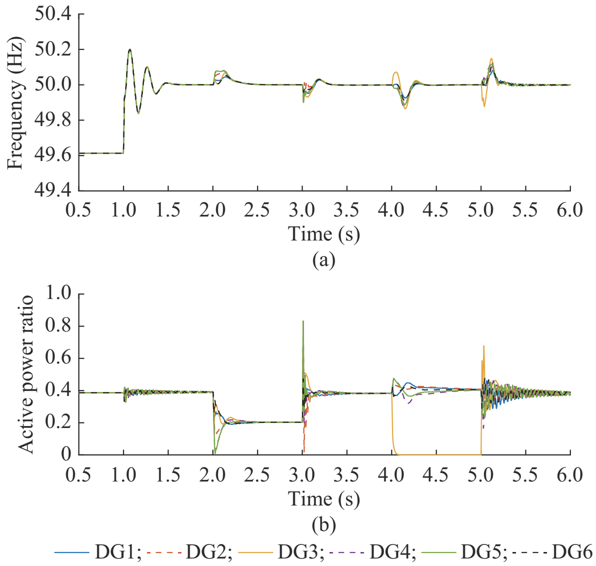

(a)

(b)

Fig. 12. Control performance under communication delay condition 2.

The proposed strategy can still perform well in addressing frequency restoration and power sharing under the short communication delay condition. Compared with the non-delay performance in Fig. 6(a), the delay performance in Fig. 11 takes a bit longer time in overshoot suppression and deviation elimination. The control results under large communication delays are given in Fig. 12. Since the communication delay is much closer to the allowable maximum delay, the frequency suffers from severe oscillations during the recovery period. In addition, after the system is subjected to a large disturbance (plug-in and out of DG3), the power appears to oscillate faster before it turns to the steady state.

E. Case 5: Performance Under Communication Failure

The test topology under communication failure is shown in Fig. 13. The communication failures occur at DG4 from $t=2$ s to $t=5$ s. Besides, load 1 is disconnected from the microgrid at $t=3$ s, while load 2 is reduced by 50% at $t=4$ s.

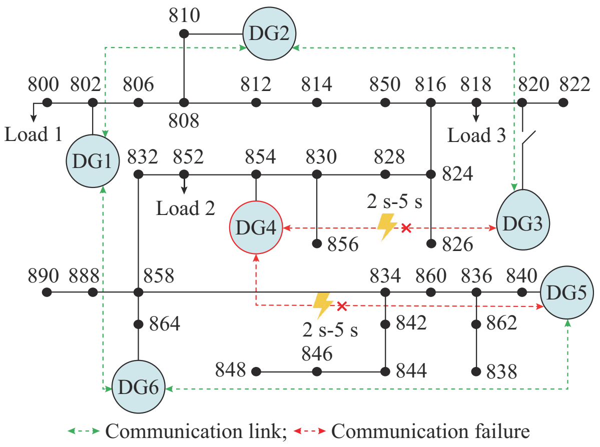

Fig. 13. Test topology under communication failure.

The control performance in Fig. 14 indicates that when the system runs stably (at $t=4$ s), the appearance of the communication failure does not affect the operation stability. However, during the communication failure period, since DG4 no longer accepts the distributed consensus information from neighbours, it no longer participates in the coordinated consensus control. Its voltage and output power deviate from consensus references when disturbances appear at $t=3$ s and $t=4$ s. Besides, since the frequency is a global quantity, the frequency of DG4 still rotates with the microgrid. After DG4 is reconnected to the communication network (at $t=5$ s), consensus tracking is resumed for frequency, voltage, and active power.

F. Case 6: Testing Under Actual PV Data

In this case, we employ actual PV data to evaluate the performance in real practice. Six PVs are integrated into the microgrid, as shown in Fig. 15. The PV outputs and the change of total load are shown in Fig. 16. The simulation timescale is scaled down to 1/100 (using 864 s instead of 86400 s a day for simulation) to facilitate data storage.

The frequency and voltage of each DG are stably controlled around the given references ($f_n=50$ Hz, $v_n=380$ V) when the proposed strategy is applied. Even when the PV outputs change drastically (from $t=200$ s to $t=500$ s), the frequency and voltage fluctuations are still rapidly suppressed in the allowable ranges. The power sharing result in Fig. 17(c) also illustrates that the proposed strategy can still maintain power sharing in complex microgrids.

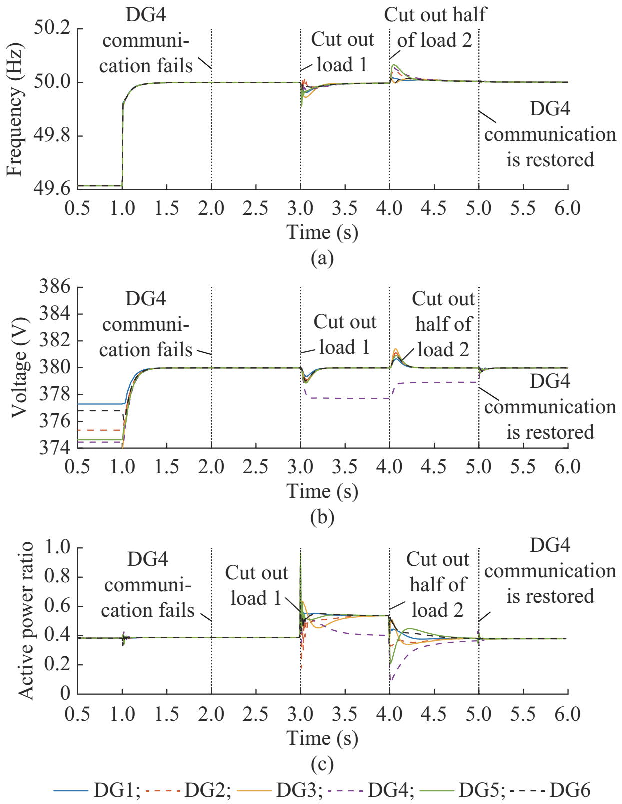

Fig. 14. Performance under communication failure. (a) Frequency. (b) Voltage. (c) Active power ratio.

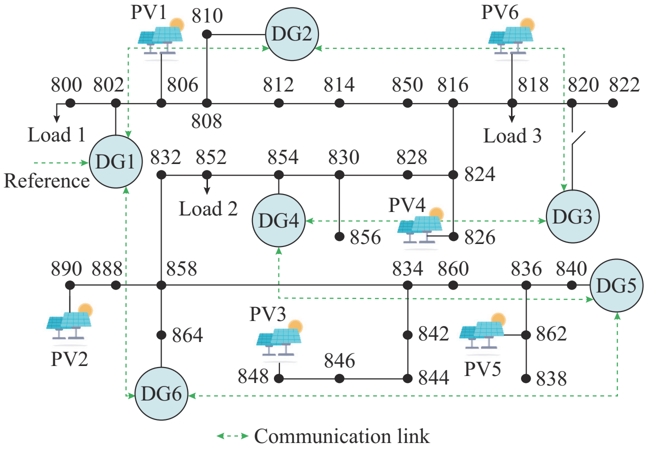

Fig. 15. Test topology with six PVs integrated.

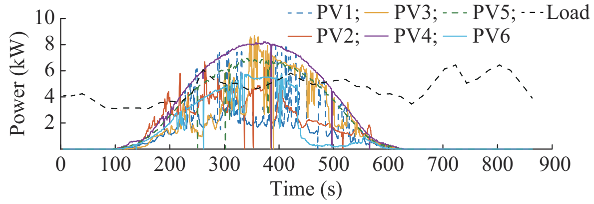

Fig. 16. PV outputs and load changes in microgrid.

Compared with our previous work [3], the proposed strategy further compensates for the damping, as shown in Fig. 18. Thus, under the same disturbance conditions, the proposed strategy in this paper has a minor overshoot and a lower rate of change of frequency (RoCoF).

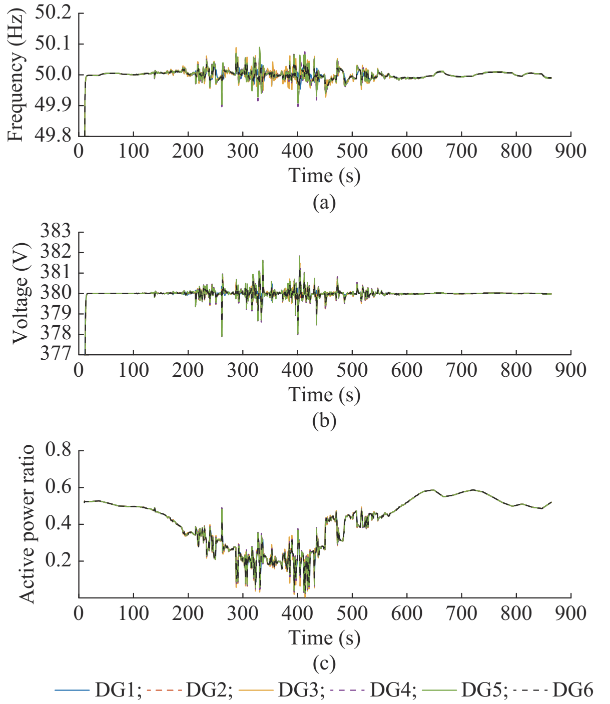

Fig. 17. Performance testing. (a) Frequency. (b) Voltage. (c) Active power ratio.

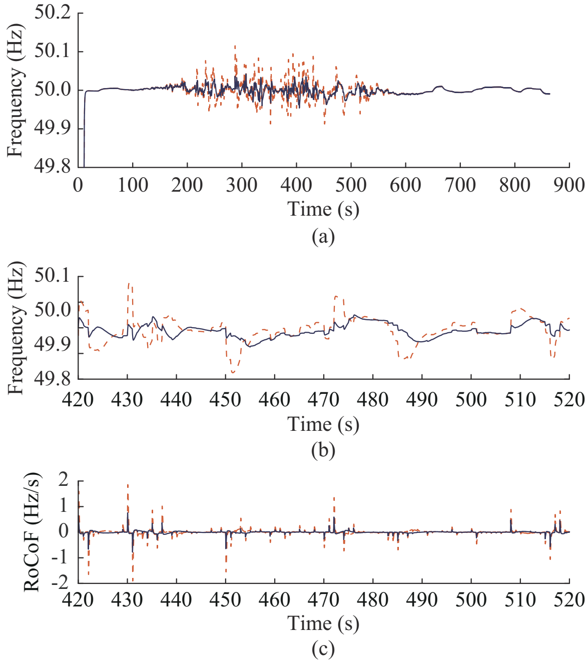

Fig. 18. Comparison of proposed strategy with previous control strategy in [3]. (a) Frequency performance throughout a day. (b) Frequency performance for a certain period of time in a day. (c) RoCoF performance for a certain period of time in a day.

The overshoot of frequency and the RoCoF are both reduced by about 50% during the period of dramatic power changes of PVs compared with previous work.

G. Case 7: Experimental Verification

Figures 19 and 20 give the control topology and experiment platform of the hardware-in-the-loop (HIL) test. The sampling frequency is 5000 Hz. The electrical circuit parameters are similar to those in [38]. The actual PV operation data are downloaded in RT-lab OP5700 to mimic the operation of the microgrid under real PV integration. Three experimental sets are as follows.

1) Set 1: general performance test, without PV integration or change of compensation parameter.

2) Set 2: performance comparison, without PV integration but with change of compensation parameter.

3) Set 3: performance under actual PV data, without change of compensation parameter.

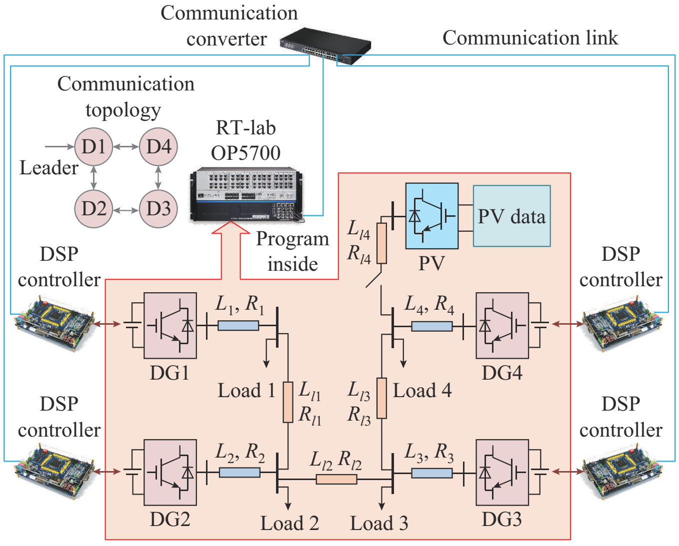

Fig. 19. Control topology of HIL test.

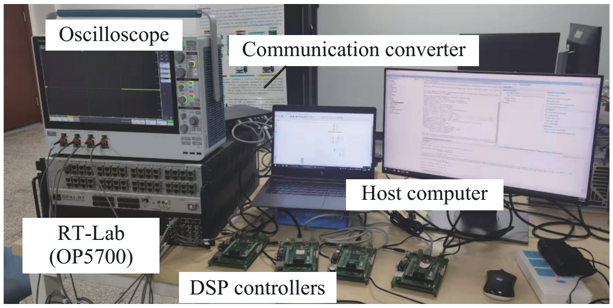

Fig. 20. Experiment platform of HIL test.

Figures 21-23 depict the general performance of this HIL test. The experimental waves exhibit similar tendencies to the results shown previously. The proposed strategy allows the voltage and frequency to fast converge to the consensus reference during disruptions. The active power sharing performance is given in Fig. 23. It can be noticed that although the disconnection and communication failure affect the power sharing performance, other remaining DGs can still rebalance the remaining power.

Figure 24 shows the performance under different inertia compensations. To evaluate the performance, we decrease the value of load 3 twice and restore it twice. The blue line shows the value of the compensated inertia, which is initially set to be non-zero and then regulated to zero.

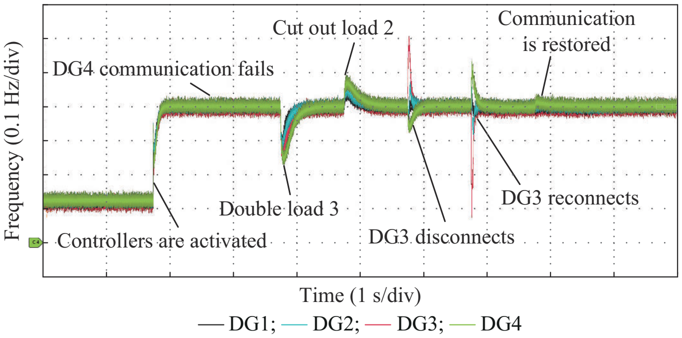

Fig. 21. Set 1: frequency control performance of HIL test.

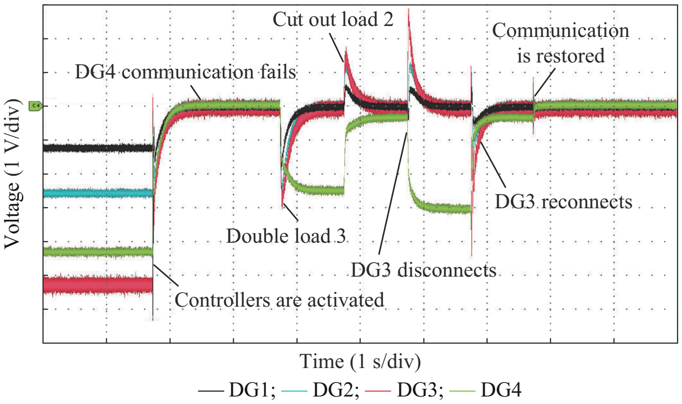

Fig. 22. Set 2: voltage control performance of HIL test.

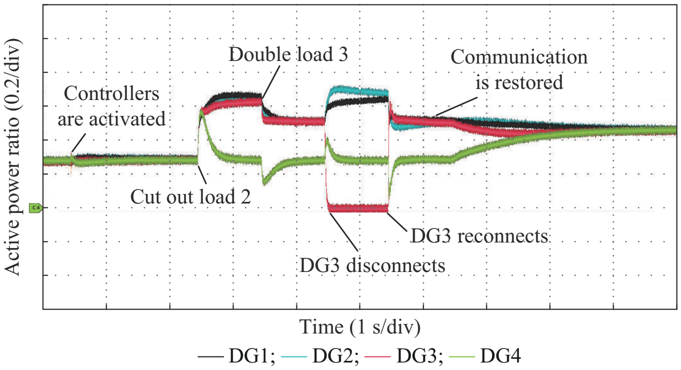

Fig. 23. Set 1: active power sharing performance of HIL test.

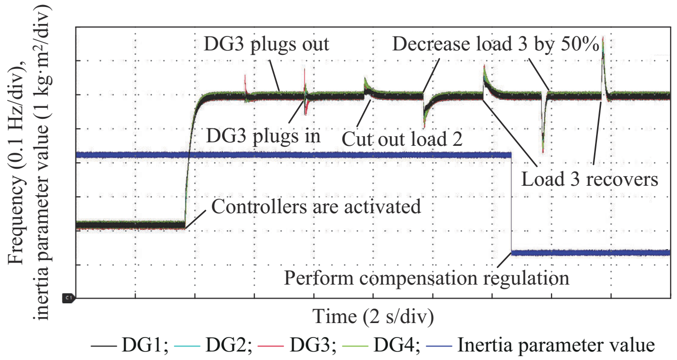

Fig. 24. Set 2: active power sharing performance of HIL test.

The control performance illustrates that the adaptive compensation can reduce the RoCoF and frequency drooping nadir when disturbances happen, which is consistent with the above simulation results.

The control performance of DG1 under PV variations is given in Fig. 25. The host computer imports 2 min PV data set to the PV converter in the RT-lab. The performance of DG1 and the PV output is given in Fig. 25. The reference and voltage are stably controlled in small ranges around the given references by the proposed strategy. The impact caused by rapid changes of PV is efficiently suppressed. The plug-and-play capacity is also validated in this scenario.

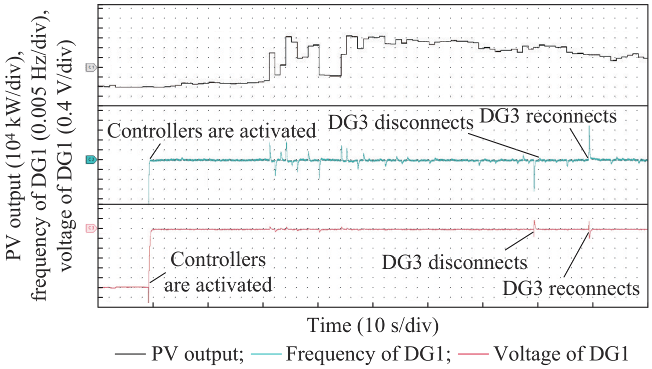

Fig. 25. Set 3: control performance of DG1 under PV variations.

V. CONCLUSION

This paper presents a novel two-level coupling-based frequency control strategy for microgrids. The proposed strategy includes a dynamic compensation algorithm to supplement inertia and damping, and an ASM-based distributed frequency consensus algorithm to address frequency restoration and power sharing. In addition, the NESO-based coupling is introduced to interconnect the control dynamics at different levels without decoupling the timescale. The stability conditions of the control system under delays are derived by applying the variation of Lyapunov functionals. The simulation and experiment results demonstrate that the proposed strategy can improve the frequency dynamics while solving frequency restorations. After a disturbance occurs in microgrid, the RoCoF, the deviation nadir of frequency, and the restoration period can all be reduced.

It is worth noting that some idealized assumptions are made in this paper for the convenience of design and proof. In future research, we plan to delve deeper into the impact of power coupling and energy saturation on the stability of distributed control implementation.

APPENDIX A

The delivered power from the i^{th} DG is:

$$P_i = \frac{V_{bi} V_i}{X_i} \sin(\delta_i - \delta_{bi}) \tag{A1}$$

where X_i is the reactance of the output connection; V_i is the voltage amplitude of the DG output point; V_{bi} is the voltage amplitude of the bus point; and δ_i and δ_{bi} are the phase angles of the DG output point and the bus point, respectively.

Combining (A1) with the dynamics (7) yields:

$$(\tau_i+\mu_0 P_F)\dot{\omega}_{di}+\mu_1\omega_{di}\dot{\omega}_{di}^2+(\mu_2 P_F+1)\omega_{di}=-A_i\sin(\delta_{di}+\delta_{ni}-\delta_{bi}) \tag{A2}$$

where $\delta_{di}=\delta_i-\delta_{ni}$ is the deviation of the phase angle; and $A_i=m_{Pi}V_{bi}V_i/X_i$ is a defined coefficient.

Define the state $[x_{i,0},x_{i,1}]^{\mathrm{T}}=[\delta_{di},\omega_{di}]^{\mathrm{T}}$. Then, we construct the following Lyapunov candidate to verify the stability of the compensation mechanism.

$$V_{ai}=\int_{\delta_{bi}-\delta_{ni}}^{x_{i,0}}A_i\sin(x_{i,0}+\delta_{ni}-\delta_{bi})\mathrm{d}x_{i,0}+\frac{1}{2\tau_i}x_{i,1}^2 \tag{A3}$$

The derivative of it can be expressed as:

$$\dot{V}_{ai}=A_i\sin(x_{i,0}+\delta_{ni}-\delta_{bi})x_{i,1}+\dot{x}_{i,1}x_{i,1}=-\mu_1\dot{x}_{i,1}^2x_{i,1}^2-(\mu_2 P_F+1)x_{i,1}^2 \tag{A4}$$

Since (A3) is positive and its differential (A4) is non-positive, the adaptive compensation can handle stable compensation.

APPENDIX B

According to the approaching law (22), we introduce the Lyapunov candidate as:

$$\boldsymbol{V}_s=(\boldsymbol{s}(t))^{\mathrm{T}}\boldsymbol{P}\boldsymbol{s}(t)+\int_{t-d}^{t}(\boldsymbol{s}(t-\alpha))^{\mathrm{T}}\boldsymbol{Q}\boldsymbol{s}(t-\alpha)\mathrm{d}\alpha+ \\ d_{\max}\int_{-d_{\max}}^{0}\int_{t+x}^{t}(\dot{\boldsymbol{s}}(x))^{\mathrm{T}}\boldsymbol{Z}\dot{\boldsymbol{s}}(x)\,\mathrm{d}\alpha\mathrm{d}x \tag{B1}$$

where $\boldsymbol{s}(t)$ is the compact form of the sliding manifold in (20); $\boldsymbol{P}$, $\boldsymbol{Q}$, and $\boldsymbol{Z}$ are the positive definite matrices; and α and x are integral states; $d_{\max}$ is the maximum delay that the system can withstand.

The derivative of $\boldsymbol{V}_s$ satisfies:

$$\dot{\boldsymbol{V}}_s=(\boldsymbol{s}(t))^{\mathrm{T}}2\boldsymbol{P}\dot{\boldsymbol{s}}(t)+(\boldsymbol{s}(t))^{\mathrm{T}}\boldsymbol{Q}\boldsymbol{s}(t)-(\boldsymbol{s}(t-d))^{\mathrm{T}}\boldsymbol{Q}\boldsymbol{s}(t-d)+ \\ d_{\max}(\dot{\boldsymbol{s}}(t))^{\mathrm{T}}\boldsymbol{Z}\dot{\boldsymbol{s}}(t)-\int_{t-d_{\max}}^{t}(\dot{\boldsymbol{s}}(x))^{\mathrm{T}}\boldsymbol{Z}\dot{\boldsymbol{s}}(x)\mathrm{d}x \tag{B2}$$

Based on (23), if $\boldsymbol{\gamma}(t-d)\left|\boldsymbol{s}(t-d)\right|\geq\vartheta\boldsymbol{I}_{N\times N}$, we have $\boldsymbol{\kappa}(\boldsymbol{\gamma}(t-d),\boldsymbol{s}(t-d))=\mathrm{sign}(\boldsymbol{s})$, and (B2) is rewritten as:

$$\dot{\boldsymbol{V}}_{s,1}\leq-\boldsymbol{s}(t)^{\mathrm{T}}2\boldsymbol{P}(\boldsymbol{r}(t-d)\boldsymbol{s}(t-d)-\boldsymbol{\eta}\boldsymbol{s}(t))+(\boldsymbol{s}(t))^{\mathrm{T}}\boldsymbol{Q}\boldsymbol{s}(t)- \\ (\boldsymbol{s}(t-d))^{\mathrm{T}}\boldsymbol{Q}\boldsymbol{s}(t-d)+d_{\max}(\boldsymbol{r}(t-d)\boldsymbol{s}(t-d)-\boldsymbol{\eta}\boldsymbol{s}(t))^{\mathrm{T}}\cdot \\ \boldsymbol{Z}(\boldsymbol{r}(t-d)\boldsymbol{s}(t-d)-\boldsymbol{\eta}\boldsymbol{s}(t))-d_{\max}^{-1}(\boldsymbol{s}(t)-\boldsymbol{s}(t-d_{\max}))^{\mathrm{T}}\cdot \\ \boldsymbol{Z}[\boldsymbol{s}(t)-\boldsymbol{s}(t-d_{\max})]\leq\boldsymbol{X}(t)^{\mathrm{T}}\begin{bmatrix}\boldsymbol{\varXi}_{11} & \boldsymbol{\varXi}_{12} & \boldsymbol{\varXi}_{13}\\ \boldsymbol{\varXi}_{12}^{\mathrm{T}} & \boldsymbol{\varXi}_{22} & \boldsymbol{\varXi}_{23}\\ \boldsymbol{\varXi}_{13}^{\mathrm{T}} & \boldsymbol{\varXi}_{23}^{\mathrm{T}} & \boldsymbol{\varXi}_{33}\end{bmatrix}\boldsymbol{X}(t) \tag{B3}$$

where $(\boldsymbol{X}(t))^{\mathrm{T}}=[(\boldsymbol{s}(t))^{\mathrm{T}},(\boldsymbol{s}(t-d))^{\mathrm{T}},(\boldsymbol{s}(t-d_{\max}))^{\mathrm{T}}]$.

$$\begin{cases}\boldsymbol{\varXi}_{11}=\boldsymbol{Q}-2\boldsymbol{P}\boldsymbol{\eta}+d_{\max}\boldsymbol{\eta}^{\mathrm{T}}\boldsymbol{\eta}\boldsymbol{Z}\\ \boldsymbol{\varXi}_{12}=(d_{\max}\boldsymbol{\eta}\boldsymbol{Z}-\boldsymbol{P})\boldsymbol{R}\\ \boldsymbol{\varXi}_{13}=\boldsymbol{Z}/d_{\max}\\ \boldsymbol{\varXi}_{22}=\boldsymbol{R}^{\mathrm{T}}\boldsymbol{R}-\boldsymbol{Q}\\ \boldsymbol{\varXi}_{23}=\boldsymbol{0}\\ \boldsymbol{\varXi}_{33}=d_{\max}\boldsymbol{Z}\\ \boldsymbol{R}=\boldsymbol{r}(t-d)\end{cases} \tag{B4}$$

where $\boldsymbol{R}$ is an auxiliary matrix. Then, if $\boldsymbol{\gamma}(t-d)\left|\boldsymbol{s}(t-d)\right|<\vartheta\boldsymbol{I}_{N\times N}$, (B2) can be written as:

$$\dot{\boldsymbol{V}}_{s,2}\leq(\boldsymbol{X}(t))^{\mathrm{T}}\boldsymbol{\varPhi}_{3\times3}\boldsymbol{X}(t) \tag{B5}$$

where the elements in matrix $\boldsymbol{\varPhi}_{3\times3}$ are given as:

$$\begin{cases}\boldsymbol{\varPhi}_{11}=\boldsymbol{Q}-2\boldsymbol{P}\boldsymbol{\eta}+d_{\max}\boldsymbol{\eta}^{\mathrm{T}}\boldsymbol{\eta}\boldsymbol{Z}\\ \boldsymbol{\varPhi}_{12}=(d_{\max}\boldsymbol{\eta}\boldsymbol{Z}-\boldsymbol{P})\boldsymbol{M}\\ \boldsymbol{\varPhi}_{13}=\boldsymbol{Z}/d_{\max}\\ \boldsymbol{\varPhi}_{22}=\boldsymbol{M}^{\mathrm{T}}\boldsymbol{M}-\boldsymbol{Q}\\ \boldsymbol{\varPhi}_{23}=\boldsymbol{0}\\ \boldsymbol{\varPhi}_{33}=d_{\max}\boldsymbol{Z}\\ \boldsymbol{M}=(\boldsymbol{r}(t-d))^{\mathrm{T}}\boldsymbol{r}(t-d)\left|\boldsymbol{s}(t-d)\right|<\vartheta\boldsymbol{r}(t-d)\end{cases} \tag{B6}$$

where $\boldsymbol{M}$ is an auxiliary matrix. Since $\boldsymbol{r}(t-d)\geq\boldsymbol{0}$, if we set $d_{\max}\boldsymbol{\eta}\boldsymbol{Z}=\boldsymbol{P}$, we can express the functions (B3) and (B5) as $\dot{\boldsymbol{V}}_{s,2}<\dot{\boldsymbol{V}}_{s,2}$. Thus, the stability issue $\dot{\boldsymbol{V}}_s<0$ turns into the proof of $\boldsymbol{\varPhi}_{3\times3}<0$, which can be satisfied by regulating the values of $\boldsymbol{\eta}$ and $d_{\max}$.

In addition, when the value of $\boldsymbol{\eta}$ is determined, the maximum delay $d_{\max}$ can be obtained by solving:

$$\begin{cases}\max d_{\max}\\ \text{s.t. } \boldsymbol{\varPhi}<\boldsymbol{0}\end{cases} \tag{B7}$$

Similar to the proof above, the microgrid with control algorithm for power sharing (29) also can be proven stable.

REFERENCE

[1] J. Fang, H. Li, Y. Tang *et al.*, "On the inertia of future more-electronics power systems," *IEEE Journal of Emerging and Selected Topics in Power Electronics*, vol. 7, no. 4, pp. 2130-2146, Dec. 2019.

[2] K. S. Ratnam, K. Palanisamy, and G. Yang, "Future low-inertia power systems: requirements, issues, and solutions–a review," *Renewable & Sustainable Energy Reviews*, vol. 124, no. 109773, pp. 1-24, Feb. 2020.

[3] C. Zhang, X. Dou, Z. Zhang *et al.*, "Inertia-enhanced distributed voltage and frequency control of low-inertia microgrids," *IEEE Transactions on Power Systems*, vol. 36, no. 5, pp. 4270-4280, Sept. 2021.

[4] U. Tamrakar, D. A. Copp, T. Nguyen *et al.*, "Optimization-based fast-frequency estimation and control of low-inertia microgrids," *IEEE Transactions on Energy Conversion*, vol. 36, no. 2, pp. 1459-1468, Jun. 2021.

[5] C. Zheng, T. Dragičević, and F. Blaabjerg, "Model predictive control-based virtual inertia emulator for an islanded alternating current microgrid," *IEEE Transactions on Industrial Electronics*, vol. 68, no. 8, pp. 7167-7177, Aug. 2021.

[6] D. Ke, C. Y. Chung, J. Xu *et al.*, "Inertia emulation uncorrelated with electromechanical dynamics to improve frequency transients using center of inertia (COI) frequency signal," *IEEE Transactions on Power Systems*, vol. 36, no. 3, pp. 1736-1749, May 2021.

[7] A. Asrari, M. Mustafa, M. Ansari *et al.*, "Impedance analysis of virtual synchronous generator-based vector controlled converters for weak ac grid integration," *IEEE Transactions on Sustainable Energy*, vol. 10, no. 3, pp. 1481-1490, Jul. 2019.

[8] H.-P. Beck and R. Hesse, "Virtual synchronous machine," in *Proceedings of 9th International Conference on Electrical Power Quality and Utilization*, Barcelona, Spain, Oct. 2007, p. 4424220.

[9] J. Chen and T. O'Donnell, "Parameter constraints for virtual synchronous generator considering stability," *IEEE Transactions on Power Systems*, vol. 34, no. 3, pp. 2479-2481, May 2019.

[10] S. Chen, Y. Sun, H. Han *et al.*, "Dynamic frequency performance analysis and improvement for parallel VSG systems considering virtual inertia and damping coefficient," *IEEE Journal of Emerging and Selected Topics in Power Electronics*, vol. 11, no. 1, pp. 478-489, Feb. 2023.

[11] D. Li, Q. Zhu, S. Lin *et al.*, "A self-adaptive inertia and damping combination control of VSG to support frequency stability," *IEEE Transactions on Energy Conversion*, vol. 32, no. 1, pp. 397-398, Mar. 2017.

[12] T. Liu, A. Chen, F. Gao *et al.*, "Double-loop control strategy with cascaded model predictive control to improve frequency regulation for islanded microgrids," *IEEE Transactions on Smart Grid*, vol. 13, no. 5,

pp. 3954-3967, Sept. 2022.

[13] P. Liu, Y. Bi, and C. Liu, "Data-based intelligent frequency control of VSG via adaptive virtual inertia emulation," *IEEE Systems Journal*, vol. 16, no. 3, pp. 3917-3926, Sept. 2022.

[14] S. Chen, Y. Sun, H. Han *et al.*, "A modified VSG control scheme with virtual resistance to enhance both small-signal stability and transient synchronization stability," *IEEE Transactions on Power Electronics*, vol. 38, no. 5, pp. 6005-6014, May 2023.

[15] H. Xiao, H. He, L. Zhang *et al.*, "Adaptive grid-synchronization based grid-forming control for voltage source converters," *IEEE Transactions on Power Systems*, doi: 10.1109/TPWRS.2023.3338967

[16] M. Chen, D. Zhou, and F. Blaabjerg, "Enhanced transient angle stability control of grid-forming converter based on virtual synchronous generator," *IEEE Transactions on Industrial Electronics*, vol. 69, no. 9, pp. 9133-9144, Sept. 2022.

[17] A. Fathi, Q. Shafiee, and H. Bevrani, "Robust frequency control of microgrids using an extended virtual synchronous generator," *IEEE Transactions on Power Systems*, vol. 33, no. 6, pp. 6289-6297, Nov. 2018.

[18] T. Kerdphol, F. S. Rahman, M. Watanabe *et al.*, "Robust virtual inertia control of a low inertia microgrid considering frequency measurement effects," *IEEE Access*, vol. 7, pp. 57550-57560, Apr. 2019.

[19] N. Sockeel, J. Gafford, B. Papari *et al.*, "Virtual inertia emulator-based model predictive control for grid frequency regulation considering high penetration of inverter-based energy storage system," *IEEE Transactions on Sustainable Energy*, vol. 11, no. 4, pp. 2932-2939, Mar. 2020.

[20] A. Fawzy, A. Bakeer, G. Magdy *et al.*, "Adaptive virtual inertia-damping system based on model predictive control for low-inertia microgrids," *IEEE Access*, vol. 9, pp. 109718-109731, Aug. 2021.

[21] X. Hou, Y. Sun, X. Zhang *et al.*, "Improvement of frequency regulation in VSG-based AC microgrid via adaptive virtual inertia," *IEEE Transactions on Power Electronics*, vol. 35, no. 2, pp. 1589-1602, Feb. 2020.

[22] Y. Khayat, Q. Shafiee, R. Heydari *et al.*, "On the secondary control architectures of AC microgrids: an overview," *IEEE Transactions on Power Electronics*, vol. 35, no. 6, pp. 6482-6500, Jun. 2020.

[23] C. Zhang, X. Dou, X. Quan *et al.*, "Distributed secondary control for island microgrids with expected dynamic performance under communication delays," *IEEE Transactions on Smart Grid*, vol. 14, no. 3, pp. 2010-2022, May 2023.

[24] B. Ning, Q. Han, and L. Ding, "Distributed finite-time secondary frequency and voltage control for islanded microgrids with communication delays and switching topologies," *IEEE Transactions on Cybernetics*, vol. 51, no. 8, pp. 3988-3999, Aug. 2021.

[25] N. M. Dehkordi, N. Sadati, and M. Hamzeh, "Fully distributed cooperative secondary frequency and voltage control of islanded microgrids," *IEEE Transactions on Energy Conversion*, vol. 32, no. 2, pp. 675-685, Jun. 2017.

[26] P. Ge, X. Dou, X. Quan *et al.*, "Extended-state-observer-based distributed robust secondary voltage and frequency control for an autonomous microgrid," *IEEE Transactions on Sustainable Energy*, vol. 11, no. 1, pp. 195-205, Jan. 2020.

[27] N. M. Dehkordi, N. Sadati, and M. Hamzeh, "Distributed robust finite-time secondary voltage and frequency control of islanded microgrids," *IEEE Transactions on Power Systems*, vol. 32, no. 5, pp. 3648-3659, Sept. 2017.

[28] X. Wu, C. Shen, and R. Iravani, "A distributed, cooperative frequency and voltage control for microgrids," *IEEE Transactions on Smart Grid*, vol. 9, no. 4, pp. 2764-2776, Jul. 2018.

[29] Z. Wang, W. Jie, M. Ma *et al.*, "Distributed event-triggered fixed-time fault-tolerant secondary control of islanded AC microgrid," *IEEE Transactions on Power Systems*, vol. 37, no. 5, pp. 4078-4093, Sept. 2022.

[30] X. Li, Q. Xu, and F. Blaabjerg, "Adaptive resilient secondary control for islanded ac microgrids with sensor faults," *IEEE Journal of Emerging and Selected Topics in Power Electronics*, vol. 9, no. 5, pp. 5239-5248, Oct. 2021.

[31] K. Mohammadi, E. Azizi, J. Choi *et al.*, "Asynchronous periodic distributed event-triggered voltage and frequency control of microgrids," *IEEE Transactions on Power Systems*, vol. 36, no. 5, pp. 4524-4538, Sept. 2021.

[32] W. Yao, Y. Wang, Y. Xu *et al.*, "Distributed weight-average-prediction control and stability analysis for an islanded microgrid with communication time delay," *IEEE Transactions on Power Systems*, vol. 37, no. 1, pp. 330-342, Jan. 2022.

[33] H. Cai, G. Hu, F. L. Lewis *et al.*, "A distributed feedforward approach to cooperative control of AC microgrids," *IEEE Transactions on Power Systems*, vol. 31, no. 5, pp. 4057-4067, Sept. 2016.

[34] G. Lou, W. Gu, Y. Xu *et al.*, "Distributed MPC-based secondary voltage control scheme for autonomous droop-controlled microgrids," *IEEE Transactions on Sustainable Energy*, vol. 8, no. 2, pp. 792-804, Apr. 2017.

[35] J. Han, "From PID to active disturbance rejection control," *IEEE Transactions on Industrial Electronics*, vol. 56, no. 3, pp. 900-906, Mar. 2009.

[36] J. Ni, L. Liu, C. Liu *et al.*, "Fast fixed-time nonsingular terminal sliding mode control and its application to chaos suppression in power system," *IEEE Transactions on Circuits and Systems II: Express Briefs*, vol. 64, no. 2, pp. 151-155, Feb. 2017.

[37] J. Lai, X. Lu, A. Monti, *et al.*, "Event-driven distributed active and reactive power dispatch for CCVSI-based distributed generators in AC microgrids," *IEEE Transactions on Industry Applications*, vol. 56, no. 3, pp. 3125-3136, Jun. 2020.

[38] C. Zhang, X. Dou, Y. Lv *et al.*, "Multi-bus-based distributed secondary voltage control for microgrids," in *Proceedings of IEEE 20th International Conference on Industrial Informatics*, Perth, Australia, Jul. 2022, pp. 146-150.

Congyue Zhang received the B.S. degree from Chien-Shiung Wu College, Southeast University, Nanjing, China, in 2017, and the Ph.D degree in electrical engineering from Southeast University, in 2023. He is currently a Postdoctoral Research Fellow with the School of Electrical Engineering, Southeast University. His research interests include modeling and control of cyber-physical system, distributed generation, microgrid, and active distribution network.

Xiaobo Dou received the B.S.E.E. degree in power system and its automation from Hohai University, Nanjing, China, in 2001, and the Ph.D. degree in power system and its automation from Southeast University, Nanjing, China, in 2006. From 2010 to 2011, he served as a Visiting Scholar at the University of Tennessee, Knoxville, USA, and Oak Ridge National Laboratory, Knoxville, USA. He is currently a Professor with the School of Electrical Engineering, Southeast University. His research interests include smart grid, microgrid, and renewable energy resource.

Jianfeng Zhao received the B.S. degree from the Huainan Mining Institute, Huainan, China, in 1995, the M.S. degree from Nanjing University of Aeronautics and Astronautics, Nanjing, China, in 1998, and the Ph. D. degree from Southeast University, Nanjing, China, in 2001. He joined the Faculty of the School of Electrical Engineering, Southeast University, where he has been a Professor since 2008. From 2014 to 2022, he was the Dean with the School of Electrical Engineering, Southeast University. He is currently the Vice President of the Nanjing Forestry University, Nanjing, China. His main research interests include utility applications of power electronics in smart grids such as solid-state transformers, active filters for power conditioning, flexible alternating current (AC) transmission system devices, multi-level AC motor drivers, and efficient energy utilization.

Qinran Hu received the B.S. degree from Chien-Shiung Wu College, Southeast University, Nanjing, China, in 2010, and the M.S. and Ph.D. degrees from the University of Tennessee, Knoxville, USA, in 2013 and 2015, respectively, all in electrical engineering. He was a Postdoctoral Fellow with Harvard University, Cambridge, USA, from 2015 to 2018. He is currently a Professor with the School of Electrical Engineering, Southeast University. His research interests include power system optimization, demand aggregation, and virtual power plant.

Xiangjun Quan received the B.S.E.E. degree in electrical engineering from Chongqing University, Chongqing, China, in 2007, and the M.Eng. and Ph.D. degrees in electrical engineering from Southeast University, Nanjing, China, in 2014 and 2018, respectively. From February 2017 to August 2017, he was with Future Renewable Electric Energy Delivery and Management (FREEDM) Systems Engineering Research Center, North Carolina State University, Raleigh, USA. From September 2017 to August 2018, he was also with the University of Texas at Austin, Austin, USA, as an Exchange Student. Since 2018, he has been an Assistant Professor with Southeast University, and an Associate Professor since 2022. His research interests include digital control techniques for converters, renewable energy generation system, and microgrid.